

# XY Network for Nuclear Segmentation in Multi-Tissue Histology Images

Simon Graham\*, *Student Member, IEEE*, Quoc Dang Vu\*, Shan E Ahmed Raza, Jin Tae Kwak<sup>+</sup> and Nasir Rajpoot<sup>+</sup>, *Senior Member, IEEE*

**Abstract**—Nuclear segmentation within Haematoxylin & Eosin stained histology images is a fundamental prerequisite in the digital pathology work-flow, due to the ability for nuclear features to act as key diagnostic markers. The development of automated methods for nuclear segmentation enables the quantitative analysis of tens of thousands of nuclei within a whole-slide pathology image, opening up possibilities of further analysis of large-scale nuclear morphometry. However, automated nuclear segmentation is faced with a major challenge in that there are several different types of nuclei, some of them exhibiting large intra-class variability such as the tumour cells. Additionally, some of the nuclei are often clustered together. To address these challenges, we present a novel convolutional neural network for automated nuclear segmentation that leverages the instance-rich information encoded within the vertical and horizontal distances of nuclear pixels to their centres of mass. These distances are then utilised to separate clustered nuclei, resulting in an accurate segmentation, particularly in areas with overlapping instances. We demonstrate state-of-the-art performance compared to other methods on four independent multi-tissue histology image datasets. Furthermore, we propose an interpretable and reliable evaluation framework that effectively quantifies nuclear segmentation performance and overcomes the limitations of existing performance measures.

**Index Terms**—Nuclear segmentation, computational pathology, deep learning.

## I. INTRODUCTION

### A. Nuclear Instance Segmentation

**H**ISTOLOGY slides enable pathologists to examine the complex structure of tissue samples at micron-level detail. Analysing digitised images of Haematoxylin and Eosin (H&E) stained tissue slides provides a unique opportunity to study macro- and micro-level tissue morphology and architecture, which serves as the ‘gold standard’ in tissue based diagnosis and prognosis today. However, whole-slide histology images are significantly large in size, typically of the size  $150K \times 100K$  pixels, containing rich information about biologically important phenomena in the tissue micro-environment. Current manual assessment suffers from low throughput and is naturally prone to intra- and inter-observer variability [1].

\* First authors contributed equally.

<sup>+</sup> Last authors contributed equally.

S.Graham and N.Rajpoot are with the Department of Computer Science, University of Warwick, UK.

S.Graham is also with the Mathematics for Real-World Systems Centre for Doctoral Training, University of Warwick, UK.

Q.D.Vu and J.T.Kwak are with the Department of Computer Science and Engineering, Sejong University, South Korea.

S.E.A.Raza is with the Centre for Evolution and Cancer & Division of Molecular Pathology, The Institute of Cancer Research, London, UK.

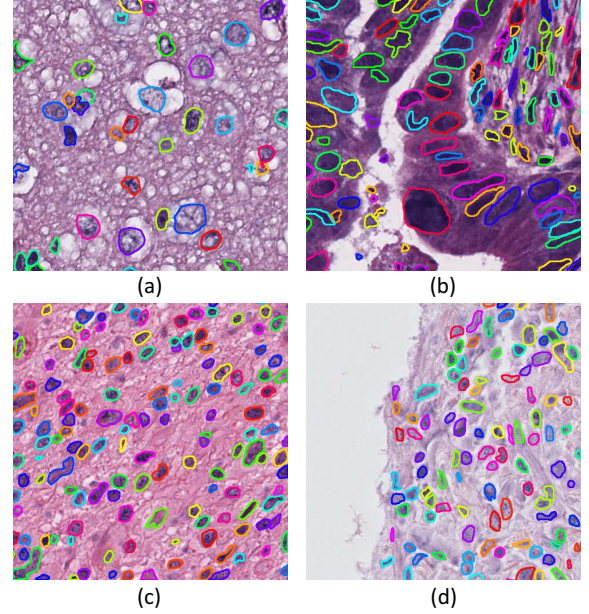


Fig. 1: Sample cropped regions extracted from each of the four datasets used in our experiments: (a) CPM-17 [2]; (b) Kumar [3]; (c) CPM-15; (d) TNBC [4].

To overcome the difficulty in visual assessment of tissue slides, there is a growing interest in Digital Pathology (DP), where digitised whole-slide images (WSIs) are acquired from glass histology slides using a scanning device. This permits efficient processing, analysis and management of the tissue specimens [5]. Each WSI contains tens of thousands of nuclei of various types, which can be further analysed in a systematic manner and used for predicting survival [6]. It has been shown that the distribution of the nuclei within an image, as well as their shape, are reliable features for diagnosing the grade and type of disease [7], [8]. However, nuclei display a high level of heterogeneity and there is significant inter- and intra-instance variability in the shape, size and chromatin pattern between and within different cell types, disease types or even from one region to another within a single tissue sample. Tumour nuclei, in particular, tend to be present in clusters, which gives rise to many overlapping instances. Due to the aforementioned difficulties, automated nuclear instance segmentation remains a challenging task. An important step towards an integrated DP workflow is to be able to detect and localise individual tissue components such as the epithelium, stroma and smooth muscle. These components possess different structural, func-

tional and chemical properties and have been shown to be related to cancer survival [9]. Therefore, localising each tissue component serves as a fundamental prerequisite for subsequent analysis. Efficient and accurate detection and segmentation of nuclei can facilitate good quality tissue segmentation (as shown in [10]), which can in turn not only facilitate the quantification of the WSIs but may also serve as an important step in understanding how each tissue component contributes to disease.

## B. Related Work

Within the current literature, energy-based methods, in particular the watershed algorithm, have been widely utilised to segment nuclear instances. For example, Yang *et al.* [11] used thresholding to obtain the markers and the energy landscape as input for watershed to extract the nuclear instances. Nonetheless, thresholding relies on a consistent difference in intensity between the nuclei and background, which does not hold for more complex images and hence often produces unreliable results. Various approaches have tried to provide an improved marker for marker-controlled watershed. Cheng *et al.* [12] used active contours to obtain the markers. Veta *et al.* [13] used a series of morphological operations to generate the energy landscape. However, these methods rely on the predefined geometry of the nuclei to generate the markers, which determine the overall accuracy of each method. Notably, Ali & Madabushi [14] avoided the trouble of refining the markers for watershed by designing a method that relies solely on the energy landscape. They combined an active contour approach with nuclear shape modelling via a level-set method to obtain the nuclear instances. Despite its widespread usage, obtaining sufficiently strong markers for watershed is a nontrivial task. Some methods have departed from the energy-based approach by utilising the geometry of the nuclei. For instance, Wienert *et al.* [15], Latorre *et al.* [16] and Kwak *et al.* [17] computed the concavity of nuclear clusters, while Liao *et al.* [18] used eclipse-fitting to separate the clusters. However, this assumes a predefined shape, which does not encompass the natural diversity of the nuclei. In addition, these methods tend to be sensitive to the choice of manually selected parameters.

Recently, deep learning methods have received a surge of interest due to their superior performance in many computer vision tasks [19], [20], [21]. These approaches are capable of automatically extracting a representative set of features, that strongly correlate with the task at hand. As a result, they are preferable to hand-crafted approaches, that rely on a selection of pre-defined features. Pioneered by the Fully Convolutional Network [22], deep convolutional neural networks have since been extensively applied to the task of segmentation within natural images and have achieved remarkable results [23], [24]. Since then, deep learning has been used within the field of DP to segment various tissue components, where in particular, deep neural networks have shown great promise in nuclear segmentation.

Since its introduction in 2015, U-Net [25], has been successfully applied to numerous segmentation tasks in medical

image analysis. The network has an encoder-decoder design, with skip connections to incorporate low-level information. U-Net treats the boundaries between instances as background and uses a weighted loss function to assist separation. However, this strategy often struggles to split instances and is highly sensitive to pre-defined parameters in the weighted loss function. A more recently proposed method in Micro-Net [26] extends U-Net by utilising an enhanced network architecture. The network processes the input at multiple resolutions and as a result, gains robustness against nuclei with varying size. Alternatively, other methods exploited the nuclear contour (or boundary) within the network. DCAN [27] proposed a dual architecture that outputs the nuclear cluster and the nuclear contour as two separate prediction maps. Instance segmentation is then achieved by subtracting the contour from the nuclear cluster prediction. They achieved the best performance in the nuclear segmentation challenge at MICCAI 2015. Cui *et al.* [28] proposed a network to predict the inner nuclear instance, the nuclear contour and the background. The network utilised a customised weighted loss function based on the relative position of pixels within the image to improve and stabilise the inner nuclei and contour prediction. Some other methods have also utilised the nuclear contour to achieve instance segmentation. For example, Kumar *et al.* [3] employed a deep learning technique for classifying the nuclei and the contours, followed by a region growing approach to extract the final instances. Khoshdeli *et al.* [29] used the contour predictions as input into a further network for segmentation refinement.

There have been various other methods to achieve instance separation. Instead of considering the contour, Naylor *et al.* [4] proposed a deep learning approach to detect superior markers for watershed by regressing the nuclear distance map. Therefore, the network avoids making a prediction for areas with indistinct contours. In [30], the authors obtained and used the posterior probability maps of the nuclear clusters to split jointly segmented nuclei. In [31], the authors developed a network that is robust to stain variations in H&E images by introducing a weighted loss function that is sensitive to the Haematoxylin intensity within the image.

In line with these developments, the field of instance segmentation within natural images is also rapidly progressing and have had a significant influence on nuclear instance segmentation methods. A notable example is Mask-RCNN [32], where their instance segmentation approach is radically different from energy-based or geometrically framed methods. Mask-RCNN achieves instance segmentation by first predicting candidate regions likely to contain an object and then deep learning based segmentation is carried out within these proposed regions. All of the aforementioned nuclear instance segmentation methods can be simplified into 1) separating the nuclei from the background and 2) separating the instances from each cluster. These two steps can be resolved either concurrently, or sequentially in no particular order.

In this paper, we propose a novel approach<sup>1</sup> that harnesses the power of fully convolutional neural networks to perform

<sup>1</sup>Model code available at: [https://github.com/vqdang/xy\\_net](https://github.com/vqdang/xy_net)

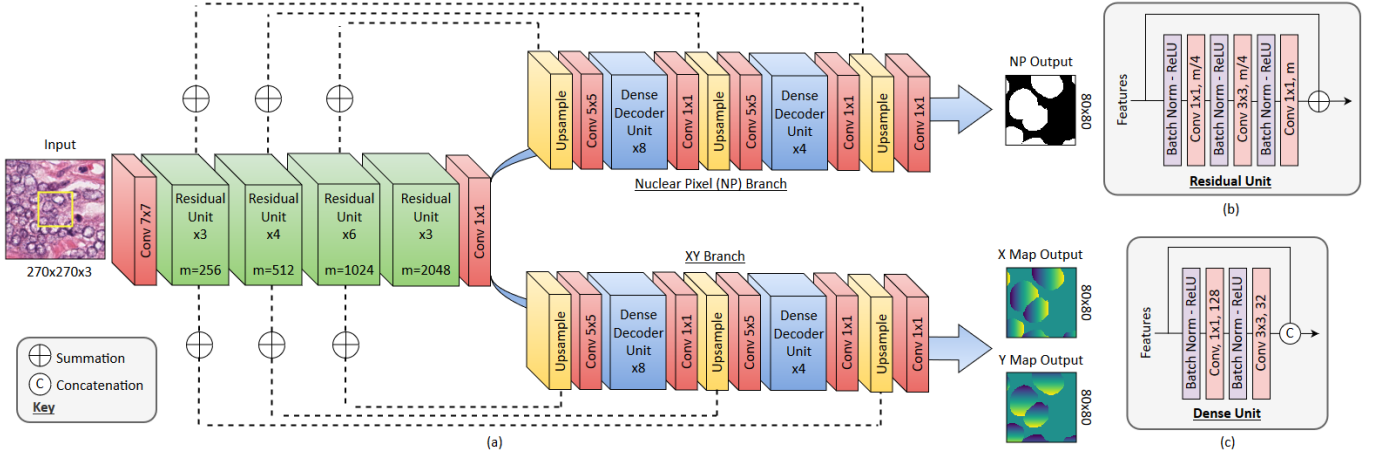


Fig. 2: (a) Overview of the network architecture,  $m$  indicates the number of feature maps within each residual unit. (b) (Pre-activated) residual unit and (c) dense unit. The yellow square within the input denotes the considered region at the output.

nuclear instance segmentation, inspired by DCAN [27]. However, instead of relying on the contour for instance separation, we argue that allowing the network to learn pixel coordinates with respect to each nuclear instance is more informative and accurate than relying on the contour alone. We propose a dual-branch network, termed as XY-Net, where one branch predicts the nuclear pixels whilst the other branch predicts the horizontal and vertical distances of nuclear pixels to their centres of mass. We show that the predicted horizontal and vertical distances of each instance can subsequently be leveraged for splitting instances from nuclear clusters via a gradient-based post-processing method. We present comparative results on four independent multi-tissue histology image datasets and demonstrate state-of-the-art performance compared to other recently proposed methods. Another contribution of this paper is an interpretable and reliable evaluation framework that effectively quantifies nuclear segmentation performance and overcomes the limitations of existing performance measures.

## II. METHODS

### A. XY Network Architecture

Nuclear segmentation is a challenging task, particularly due to the high level of inter- and intra-class heterogeneity and the presence of clustered nuclei. In order to extract a strong and representative set of features, we employ a sufficiently deep neural network. Specifically, we use a variant of the pre-activated residual network with 50 layers [33] (Preact-ResNet50), due to its excellent performance in recent computer vision tasks [34] and robustness against input perturbation [35]. Compared to the standard Preact-ResNet50 implementation, we reduce the total down-sampling factor from 32 to 8 by using a stride of 1 in the first convolution and removing the subsequent max-pooling operation. This ensures that there is no immediate loss of information that is important for performing an accurate segmentation. Various residual units are applied throughout the network at different down-sampling levels. A series of consecutive residual units is denoted as a residual block. The number of residual units within each

residual block is 3, 4, 6 and 3 that are applied at down-sampling levels 1, 2, 4 and 8 respectively. For clarity, a down-sampling level of 2 means that the input has a reduction in the spatial resolution by a factor of 2.

Following Preact-ResNet50, we perform nearest neighbour up-sampling via two distinct branches to obtain accurate nuclear instance segmentation. We name the corresponding branches: (i) nuclear pixel (NP) and (ii) XY branch. The NP branch predicts whether or not a pixel belongs to the nuclei or background, whereas the XY branch predicts the horizontal and vertical distances of nuclear pixels to their centres of mass. In other words, the NP branch separates nuclear pixels from the background, whilst the XY branch helps determine how to split the touching nuclei. In this way, we build an instance-aware network that independently achieves the two tasks of nuclear instance segmentation. Both up-sampling branches utilise the same architectural design, which consists of a series of up-sampling operations and densely connected units [36] (or dense units). Similar to the residual unit of Preact-ResNet50, the dense unit ensures efficient gradient propagation. In addition, by stacking multiple and relatively cheap dense units, we build up a large receptive field with minimal parameters, compared to using a single convolution with a larger kernel size. Similar to U-Net, we use skip connections to incorporate features from the encoder, but utilise summation as opposed to concatenation. The consideration of low-level information is particularly important in segmentation tasks, where we aim to precisely delineate the object boundaries. We use dense units

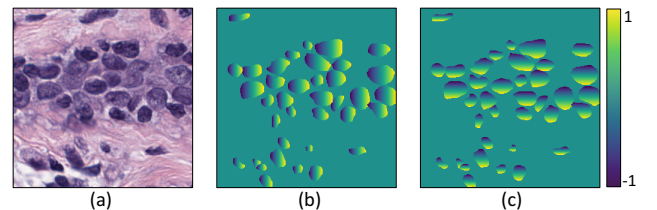


Fig. 3: (a) Cropped original image; (b) X map label; (c) Y map label.



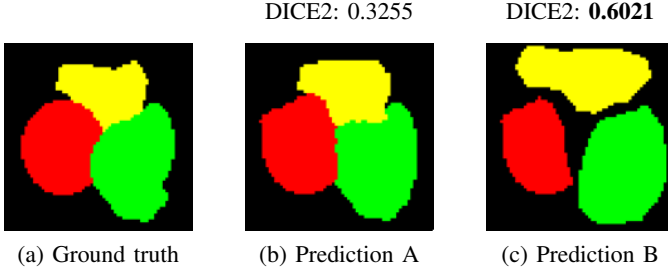


Fig. 4: Examples highlighting the effect of Ensemble Dice (DICE2) with varying predictions.

after the first and second up-sampling operation, where the number of units is 4 and 8 respectively. Valid convolution is performed throughout the two up-sampling branches to prevent boundary-effects. This results in the size of the output being smaller than that of the input.

We display an overview of the network architecture in Fig. 2a, where the spatial dimension of the input is  $270 \times 270$ , while the output is  $80 \times 80$ . We show a residual unit and a dense unit within Fig. 2b and Fig. 2c. We denote  $m$  as the number of feature maps within each convolution of a given residual unit. At each down sampling level, from left to right,  $m=256, 512, 1024, 2048$  respectively. We keep a fixed amount of feature maps within each dense unit throughout the two branches as shown in Fig. 2c.

### B. Loss Function

The proposed design has 3 different sets of weights:  $w_0$ ,  $w_1$  and  $w_2$  which refer to the weights of the Preact-ResNet50 encoder, the NP branch decoder and the XY branch decoder respectively. These 3 sets of weights are optimised together using the loss  $\mathcal{L}$  defined as:

$$\mathcal{L} = \mathcal{L}_a + \mathcal{L}_b + \mathcal{L}_c + \mathcal{L}_d \quad (1)$$

where  $\mathcal{L}_a$  and  $\mathcal{L}_b$  represent the classification loss with respect to the output at the NP branch, while  $\mathcal{L}_c$  and  $\mathcal{L}_d$  represents the regression loss with respect to the output of the XY branch.

Given the input image  $I$ , at each pixel  $i$  we define  $p_i(I, w_0, w_1)$  as the pixel-based softmax classification output of the NP branch,  $q_i(I, w_0, w_2)$  as the regression output of the XY branch with  $\Psi_i(I)$  and  $\Gamma_i(I)$  as their respective ground truth (GT). An example of the target output that we aim to predict at the output of the XY branch is given in Fig. 3.  $\Psi_i(I)$  is the nuclear binary map GT, while  $\Gamma_i(I)$  denotes the GT of the distances of nuclear pixels to their corresponding centres of mass. Specifically, we assign values between -1 and 1 to nuclear pixels independently of the horizontal and vertical directions. We assign the value of the background and the line crossing the centre of mass within each nucleus to be 0. For clarity, we denote the horizontal and vertical components of the GT XY map as X map  $\Gamma_{i,x}$  and Y map  $\Gamma_{i,y}$  respectively.

At the output of NP branch, we calculate both the binary cross entropy loss  $\mathcal{L}_a$  and the soft Sorenson dice loss  $\mathcal{L}_b$  between the output of the NP branch and the GT. These two

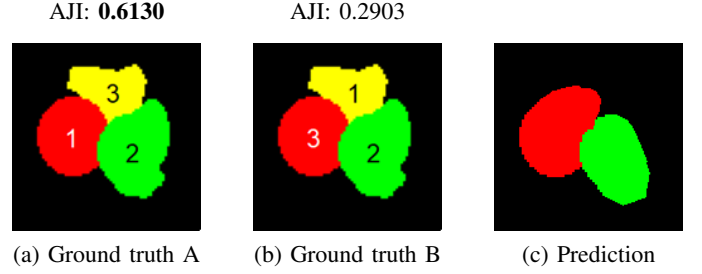


Fig. 5: Examples highlighting the effect of AJI with varying ground truth.

losses are then added together to give the overall classification loss. Concretely, we define  $\mathcal{L}_a$  and  $\mathcal{L}_b$  as:

$$\mathcal{L}_a = -\frac{1}{n} \sum_{i=1}^N \sum_{k=1}^K \Psi_{i,k}(\mathbf{I}) \log p_{i,k}(\mathbf{I}; \mathbf{w}_0, \mathbf{w}_1) \quad (2)$$

$$\mathcal{L}_b = 1 - \frac{2 \times \sum_{i=1}^N (p_i(\mathbf{I}; \mathbf{w}_0, \mathbf{w}_1) \times \Psi_i(\mathbf{I})) + \epsilon}{\sum_{i=1}^N p_i(\mathbf{I}; \mathbf{w}_0, \mathbf{w}_1) + \sum_{i=1}^N \Psi_i(\mathbf{I}) + \epsilon} \quad (3)$$

with  $\epsilon$  is a smoothness constant which we set to  $1.0e^{-3}$ .  $K$  denotes the number of classes which is two in our case (nuclei and background pixel).

At the output of the XY branch, we compute a multiple term regression loss. We denote  $\mathcal{L}_c$  as the mean squared error between the predicted horizontal and vertical distances and the GT.  $\mathcal{L}_d$  calculates the mean squared error between the horizontal and vertical gradients of the X and Y maps respectively and the corresponding gradients of the GT. We formally define  $\mathcal{L}_c$  and  $\mathcal{L}_d$  as:

$$\mathcal{L}_c = \frac{1}{n} \sum_{i=1}^N (q_i(\mathbf{I}; \mathbf{w}_0, \mathbf{w}_2) - \Gamma_i(\mathbf{I}))^2 \quad (4)$$

$$\mathcal{L}_d = \frac{1}{M} \sum_{i \in \text{nuclei}} (\nabla_x(q_{i,x}(\mathbf{I}; \mathbf{w}_0, \mathbf{w}_2)) - \nabla_x(\Gamma_{i,x}(\mathbf{I})))^2 + \frac{1}{M} \sum_{i \in \text{nuclei}} (\nabla_y(q_{i,y}(\mathbf{I}; \mathbf{w}_0, \mathbf{w}_2)) - \nabla_y(\Gamma_{i,y}(\mathbf{I})))^2 \quad (5)$$

Within equation (5),  $\nabla_x$  and  $\nabla_y$  denote the gradient in the horizontal  $x$  and vertical  $y$  directions respectively while  $M$  denotes the total number of nuclei pixels within ground truth.

### C. Gradient-based Post-processing

Within each X and Y map, pixels between separate instances have a significant difference. As a result, any edge detection method can potentially inform where the nuclei should be separated. We define

$$S_m = \max(H_x(q_x), H_y(q_y)) \quad (6)$$

where  $S_m$  outlines the nuclear contours and  $H$  denotes edge detection. In our case, we choose to use Sobel for simplicity and efficiency, hence the name gradient-based post-processing. We compute markers  $M = \sigma(\tau_h(p) - \tau_k(S_m))$ .  $\tau$  is a threshold function which set values above empirically selected values

$h$  and  $k$  to 1 or 0 otherwise.  $\sigma$  is a rectifier that sets all negative values to 0. We obtain the energy landscape  $E = [1 - \tau_k(S_m)] * \tau_h(p)$ . Finally,  $M$  is used as the marker during marker-controlled watershed to determine how to split  $\tau_h(p)$ , given the energy landscape  $E$ .

#### D. Evaluation Metrics

As mentioned in Section I, the task of nuclear instance segmentation can be divided into two main steps: 1) separating the nuclei from the background and 2) separating the individual nuclei from each cluster. We can further break down these two steps to give the following three sub-tasks:

- Separate the nuclei from the background
- Detect individual nuclear instances
- Segment each detected instance

To achieve accurate nuclear segmentation, the evaluation metrics should also take into account these three sub-tasks. Current evaluation metrics, however, do not reflect well the task of nuclear instance segmentation. In fact, a quantitative measurement of instance segmentation should not only tell whether one approach is superior, but the measurement should also indicate which sub-task the method performs particularly well on. In the current literature, two evaluation metrics have been mainly adopted to quantitatively measure the performance of nuclear instance segmentation: 1) Ensemble Dice (DICE2) [2], and 2) Aggregated Jaccard Index (AJI) [3]. Given the GT  $X$  and prediction  $Y$ , DICE2 computes and aggregates DICE per nucleus, where Dice coefficient (DICE) is defined as  $2 \times (X \cap Y) / (|X| + |Y|)$  and AJI computes the ratio of an aggregated intersection cardinality and an aggregated union cardinality between  $X$  and  $Y$ . DICE2 and AJI were utilised as the metrics at two nuclear instance segmentation challenges at the MICCAI conference in recent years [2], [37]. Although these metrics aimed to assess the second and/or third sub-tasks, they are limited in many ways, and thus they may not facilitate a fair comparison between methods. Hereby, we discuss some major limitations of each of the two metrics.

**Ensemble Dice;** This metric over penalises predictions that overlap with multiple GT segments. We illustrate this problem in Fig. 4. At first glance, it is apparent that prediction A (Fig. 4b) is superior compared to prediction B (Fig. 4c). However, each segment in prediction A overlaps with multiple segments in the GT. As a result, each time a predicted segment is used to calculate DICE, it receives a penalty, not just from the largest GT segment it intersects with (likely to be the corresponding GT), but also from neighbouring segments in the GT which it overlaps with. On the other hand, prediction B contains far more false negative predictions, but each predicted segment only intersects with only one GT segment. Hence, it obtains a higher overall score of 0.6021 compared to a score of 0.3255 obtained by prediction A.

**Aggregated Jaccard Index;** For each GT segment, this metric finds the best matching predicted segment, updates the score and removes it from further calculation. Thus, it may not compute the score using the optimal pairing between the GT and predicted segments. For this reason, AJI greatly depends on the ordering of the instances in the GT, especially within

each nuclear cluster. Therefore, AJI is permutation-variant and suffers from poor reproducibility. This phenomenon is illustrated as in Fig. 5. We denote the numbering within each GT segment that indicates the order of calculation. Then, by changing the numbering of the GT from Fig. 5a to Fig. 5b, the AJI score changes significantly. In the above example the score changes from 0.6130 to 0.2903 with a different ordering of GT segments.

It is clear that DICE2 is not a reliable quantitative measurement. On the other hand, AJI appears to be a better metric because it avoids the over penalisation problem of DICE2 by considering only one GT segment for each predicted segment. Even still, due to its lack of permutation invariance, AJI should also not be used as a single performance measure to compare different results. To improve AJI, we propose a modified version called  $AJI^+$  that is permutation invariant. The original AJI is permutation variant since it has no assumption on the ordering of the GT segments. To achieve permutation invariance,  $AJI^+$  sorts the GT segments by their size before the AJI calculation.

**Panoptic Quality;** We propose to use another metric for accurate quantification and interpretability to assess the performance of nuclear instance segmentation. Originally proposed in [38], Panoptic Quality (PQ) for nuclear instance segmentation is defined as:

$$PQ = \underbrace{\frac{|TP|}{|TP| + \frac{1}{2}|FP| + \frac{1}{2}|FN|}}_{\text{Detection Quality(DQ)}} \times \underbrace{\frac{\sum_{(p,g) \in TP} IoU(p,g)}{|TP|}}_{\text{Segmentation Quality(SQ)}} \quad (7)$$

where  $g$  denotes a GT segment and  $p$  denotes a prediction segment. Each  $(p,g)$  pair is mathematically proven to be *unique* [38] over the entire set of prediction and GT segments if their  $IoU(p,g) > 0.5$ . This condition guarantees PQ from falling into the pitfall of AJI, regardless of the ordering of both GT and prediction segments. The unique matching splits all available segments into matched pairs (TP), unmatched GT segments (FN) and unmatched prediction segments (FP). From this, PQ can be intuitively analysed as follows: the *detection quality* (DQ) is the  $F_1$  Score that is widely used to evaluate instance detection, while *segmentation quality* (SQ) can be interpreted as how close each correctly detected instance is to their matched GT. DQ and SQ, in a way, also provide a direct insight into the second and third sub-tasks, defined above. We believe that PQ should set the standard for measuring the performance of nuclear instance segmentation methods.

To fully characterise and understand the performance of each method we use the following three metrics: 1) DICE to measure the separation of all nuclei from the background; 2) Panoptic Quality as a unified score for comparison and 3)  $AJI^+$  for legacy comparison<sup>2</sup>. Panoptic quality is further broken down into DQ and SQ components for interpretability. Note, SQ is calculated only within true positive segments and should therefore be observed together with DQ.

<sup>2</sup>Evaluation code available at: <https://github.com/vqdang/src/metrics>

TABLE I: Comparative experiments on the CPM-17 [2] and Kumar [3] datasets. For Kumar, We split the test sets into same tissue (ST) and different tissue (DT) test sets, in the same fashion as [3]. We display results with and without stain normalisation.

		CPM-17					Kumar-ST					Kumar-DT				
		DICE	AJI <sup>+</sup>	DQ	SQ	PQ	DICE	AJI <sup>+</sup>	DQ	SQ	PQ	DICE	AJI <sup>+</sup>	DQ	SQ	PQ
No Stain Normalisation	FCN8 [22]	0.808	0.517	0.749	0.619	0.469	0.732	0.357	0.424	0.687	0.297	0.541	0.265	0.241	0.642	0.160
	FCN8 + WS [22]	0.808	0.573	0.753	0.672	0.512	0.732	0.426	0.521	0.686	0.364	0.541	0.292	0.283	0.641	0.188
	U-Net [25]	0.821	0.611	0.775	0.728	0.569	0.768	0.432	0.524	0.732	0.386	0.633	0.314	0.325	0.697	0.235
	U-Net + WS [25]	0.821	0.625	0.772	0.736	0.574	0.768	0.476	0.590	0.732	0.436	0.633	0.343	0.366	0.692	0.263
	SegNet [39]	0.862	0.641	0.797	0.778	0.622	0.776	0.430	0.541	0.715	0.388	0.786	0.439	0.514	0.737	0.383
	SegNet + WS [39]	0.862	0.688	0.800	0.812	0.652	0.776	0.516	0.662	0.722	0.479	0.786	0.499	0.594	0.739	0.443
	DCAN [27]	0.811	0.618	0.746	0.764	0.575	0.748	0.457	0.598	0.698	0.424	0.649	0.308	0.362	0.675	0.254
	Mask-RCNN [32]	0.850	0.694	0.792	0.838	0.666	0.769	0.562	0.706	0.714	0.507	0.783	0.575	0.728	0.706	0.517
	Micro-Net [26]	0.857	0.682	0.823	0.791	0.653	0.791	0.583	0.716	0.733	0.526	0.792	0.586	0.669	0.739	0.496
	DIST [4]	0.828	0.639	0.710	0.753	0.538	0.783	0.577	0.643	0.725	0.468	0.793	0.571	0.595	0.727	0.437
XY-Net	0.869	0.709	0.845	0.813	<b>0.690</b>	0.817	0.618	0.785	0.757	<b>0.596</b>	0.831	0.626	0.727	0.775	<b>0.569</b>	
Stain Normalisation	FCN8 [22]	0.806	0.525	0.749	0.632	0.479	0.720	0.361	0.419	0.685	0.290	0.668	0.325	0.313	0.663	0.210
	FCN8 + WS [22]	0.806	0.579	0.753	0.685	0.522	0.720	0.424	0.506	0.686	0.352	0.668	0.367	0.367	0.664	0.245
	U-Net [25]	0.827	0.616	0.779	0.748	0.587	0.769	0.414	0.513	0.731	0.379	0.725	0.345	0.411	0.720	0.300
	U-Net + WS [25]	0.827	0.634	0.780	0.752	0.591	0.769	0.469	0.590	0.730	0.435	0.725	0.414	0.475	0.715	0.345
	SegNet [39]	0.862	0.657	0.799	0.795	0.636	0.767	0.422	0.530	0.708	0.375	0.804	0.464	0.542	0.744	0.406
	SegNet + WS [39]	0.862	0.693	0.802	0.813	0.653	0.767	0.496	0.634	0.715	0.454	0.804	0.524	0.618	0.745	0.463
	DCAN [27]	0.815	0.625	0.748	0.771	0.581	0.734	0.451	0.594	0.710	0.426	0.673	0.364	0.416	0.700	0.295
	Mask-RCNN [32]	0.848	0.687	0.790	0.824	0.652	0.768	0.562	0.704	0.705	0.499	0.781	0.580	0.726	0.713	0.518
	Micro-Net [26]	0.858	0.685	0.828	0.788	0.654	0.784	0.578	0.701	0.735	0.516	0.786	0.580	0.664	0.737	0.491
	DIST [4]	0.831	0.629	0.695	0.764	0.532	0.786	0.583	0.661	0.720	0.477	0.788	0.568	0.607	0.718	0.437
XY-Net	0.868	0.700	0.837	0.808	<b>0.677</b>	0.820	0.622	0.798	0.761	<b>0.607</b>	0.838	0.639	0.748	0.771	<b>0.581</b>	

### III. EXPERIMENTS AND RESULTS

#### A. Datasets

For this study, we utilise four independent multi-tissue H&E stained image datasets which we refer to as Kumar [3], CPM-15, CPM-17 [2] and TNBC [4]. All images from these datasets have complete associated pixel-level nuclear annotations. Example images from each of the four datasets are displayed in Fig. 6.

Kumar is an open source dataset, initially used in [3], and consists of 30 image tiles of size 1,000×1,000 pixels from seven organs (6 breast, 6 liver, 6 kidney, 6 prostate, 2 bladder, 2 colon and 2 stomach). The image tiles originate from The Cancer Genome Atlas (TCGA) database and are acquired at 40× magnification.

The image tiles in CPM-15 and CPM-17 are also taken from the TCGA database. However, they were both used as part of the Computational Precision Medicine Nuclear Segmentation Challenge (CPM) at MICCAI 2015 and MICCAI 2017 respectively. CPM-15 contains 15 image tiles of variable size ranging from 400×400 to 1000×600 pixels and are acquired at 40× magnification. These 15 image tiles make up the training set of the CPM-15 challenge. CPM-17 contains a total of 64 image tiles which consist of the combination of both the training and testing sets used in the 2017 challenge. The image tiles in CPM-17 have a size ranging from 500×500 to 600×600 pixels and are acquired at either 20× or 40× magnification.

The TNBC dataset [30] is collected from the Curie Institute, consisting of 50 annotated H&E stained histology images of size 512×512 pixels at 40× magnification. Tiles are taken from eleven patients from a cohort of Triple Negative Breast Cancer (TNBC) patients. In contrast to TCGA where image

tiles are taken from frozen tissue specimens, images within TNBC were prepared from paraffin preserved samples instead.

#### B. Implementation and Training Details

We implemented our framework with the open source software library TensorFlow version 1.8.0 [40]. During training, data augmentation including flip, rotation, Gaussian blur and median blur was applied to all methods. All networks received an input patch with a size ranging from 252×252 to 270×270. This size difference is due to the use of valid convolutions in some architectures, such as XY-Net and U-Net. Regarding XY-Net, we initialised the model with pre-trained weights on the ImageNet dataset [34], trained only the decoders for the first 50 epochs, and then fine-tuned all layers for another 50 epochs. We used Adam optimisation with an initial learning rate of  $10^{-4}$  and then reduced it to a rate of  $10^{-5}$  after 25 epochs. This strategy was repeated for fine-tuning. In all experiments, a batch size of 8 was used. The network was trained with an RGB input, normalised between 0 and 1.

#### C. Comparative Analysis of Segmentation Methods

**Experimental Setting:** We evaluated our approach by comparing it to several other segmentation methods including FCN8 [22], U-Net [25], SegNet [39], DCAN [27], Mask-RCNN [32], Micro-Net [26] and DIST [4]. We also analysed the synergy between stain normalisation (SN) and colour augmentation (CA) techniques when training the neural networks with H&E stained images. Despite their widespread usage, it's relatively unclear how each technique contributes to the overall model performance. Understanding the effect of each technique will help drive forward future research. Therefore, we conducted a large-scale experiment to compare

TABLE II: Comparative experiments on the TNBC [4] test set to evaluate different stain normalisation training and testing strategies, with and without colour augmentation. During training, models use *No* or *Single* stain normalisation. During testing, models use *No*, *Single* or *Multi* stain normalisation strategies.

		With Colour Augmentation					Without Colour Augmentation				
Train	Test	DICE	AJI <sup>+</sup>	DQ	SQ	PQ	DICE	AJI <sup>+</sup>	DQ	SQ	PQ
<i>No</i>	<i>No</i>	0.698	0.530	0.670	0.769	0.519	0.588	0.422	0.570	0.757	0.436
<i>No</i>	<i>Single</i>	0.794	0.627	0.752	0.773	0.583	0.754	0.550	0.671	0.760	0.512
<i>No</i>	<i>Multi</i>	0.803	0.643	0.766	0.779	<b>0.599</b>	0.777	0.586	0.716	0.770	<b>0.554</b>
<i>Single</i>	<i>No</i>	0.719	0.557	0.692	0.770	0.536	0.423	0.282	0.425	0.720	0.315
<i>Single</i>	<i>Single</i>	0.765	0.593	0.728	0.776	0.567	0.724	0.515	0.648	0.749	0.488
<i>Single</i>	<i>Multi</i>	0.783	0.615	0.741	0.781	0.581	0.733	0.524	0.659	0.751	0.498

TABLE III: Comparative experiments on the Combined CPM [2] and TNBC [4] dataset. Models are first trained on the Kumar training set with no stain normalisation. Best models on Kumar validation are picked to make predictions with a multi stain normalisation strategy. For conciseness, we disregard semantic segmentation approaches without watershed processing.

	CPM					TNBC				
	DICE	AJI <sup>+</sup>	DQ	SQ	PQ	DICE	AJI <sup>+</sup>	DQ	SQ	PQ
FCN8 + WS [22]	0.747	0.545	0.646	0.694	0.454	0.738	0.545	0.627	0.726	0.458
U-Net + WS [25]	0.811	0.629	0.753	0.756	0.573	0.763	0.591	0.683	0.767	0.526
SegNet + WS [39]	0.773	0.585	0.726	0.722	0.528	0.758	0.584	0.693	0.746	0.521
DCAN [27]	0.789	0.580	0.728	0.730	0.535	0.730	0.532	0.635	0.721	0.463
Mask-RCNN [32]	0.793	0.621	0.793	0.750	0.597	0.756	0.594	0.758	0.772	0.589
Micro-Net [26]	0.785	0.611	0.643	0.740	0.480	0.714	0.546	0.545	0.743	0.409
DIST [4]	0.774	0.575	0.618	0.716	0.447	0.711	0.529	0.544	0.741	0.405
XY-Net	0.828	0.656	0.781	0.784	<b>0.615</b>	0.803	0.643	0.766	0.779	<b>0.599</b>

the combination of various SN and CA training and testing strategies.

To allow straight forward future comparison with our method, we utilised CPM-17 and Kumar, which are two large and well annotated datasets, for this experiment. Similar to Kumar *et al.* [3], we split the Kumar dataset into three different sub-datasets: (i) Kumar-Train, a training set with 16 image tiles (4 breast, 4 liver, 4 kidney and 4 prostate); (ii) Kumar-ST, a testing set with 8 image tiles (2 breast, 2 liver, 2 kidney and 2 prostate) that are of the same tissue types as those in Kumar-Train and (iii) Kumar-DT, a testing set with 6 image tiles (2 bladder, 2 colon, 2 stomach) that are of different tissue types to those used in Kumar-Train. Despite adhering to the dataset split as closely as possible, Kumar *et al.* [3] did not provide the exact image breakdown. Therefore to encourage reproducibility, we provide our dataset split<sup>3</sup>. For CPM-17, we utilised the same split that had been employed for the challenge.

**Comparative Results;** Table I shows detailed results of this experiment. A large variation in performance between methods within each dataset is observed, particularly for the Kumar-DT dataset. The comparison also favours methods incorporating strong instance-aware techniques. Networks built only for semantic segmentation like FCN8 and SegNet suffer from low PQ values. However, these methods obtain a better segmentation when combined with watershed. Meanwhile, weak instance-aware methods that utilise a weighted loss depend greatly on the capacity of the network. This is reflected by the low performance U-Net and the competitive performance

of Micro-Net. Hence, we also incorporate watershed with U-Net to assist with instance separation. On the other hand, given the same method, there is also a large difference between the Kumar and CPM-17 dataset. This indicates that Kumar-ST and Kumar-DT contain more complex samples, compared to the test set of CPM-17, with a greater number of overlapping nuclei. We also observe that SN leads to a small increase in performance of each method, when trained with CA. This boost is particularly visible for Kumar-DT, where the stain variability is greater. XY-Net exhibits superior performance compared to all other competing methods on all reported statistical measures, under various conditions.

#### D. Stain Normalisation and Colour Augmentation

**Experimental Setting;** The above comparative study sheds some light on the effect of SN with CA. However, it is unknown how much CA contributes to the overall result. The effect of SN is also unclear under the presence of significant stain variation. Therefore, we performed a thorough analysis with multiple combinations of SN and CA, during both training and testing. To limit the computational expense, this experiment was conducted with our approach as the main focus and the model was trained on Kumar-Train. To assess how the model coped with stain variation, we adopted the combined Kumar-ST and Kumar-DT as the validation set and TNBC as the test set. We chose to process TNBC as a test set because these images were obtained from a different source and have a significantly different stain appearance. In this experiment, we denote *Single* as SN with one target image, whereas *Multi* applies SN to multiple targets to create multiple

<sup>3</sup>Dataset information available at :<https://github.com/vqdang/data>



transformed images. When utilising the Multi strategy, we picked four images within the Kumar-Train dataset that have a radically different stain as targets and then combined the predictions.

**Comparative Results;** Table II reports the results of various SN training and testing strategies. Using SN within training-testing gives a more stable performance, reflected by a 0.058 difference in PQ between *No-No* and *Single-Single*. However, after closer inspection, the benefit of utilising SN during test time is much more apparent, indicated by the improved SQ in *No-Single*, *No-Multi* and *Single-Multi*. The best performing model was obtained with *No* SN during training and *Multi* SN during testing. Notably, *No-Single* even beats *Single-Single* by a fairly large margin of 0.016 in PQ. These results strongly suggest that this strategy helps to deal with stain variation in histology images. These observations suggest that training with SN reduces the stain variability and, in turn, may decrease the robustness of the model with the presence of extreme stain variation. The result also demonstrates that it is imperative to use CA during training. To build a model that transitions well to new data, with a potentially different stain, we choose to use *No* SN during training and the *Multi* SN approach during testing.

#### E. Generalisation Study

**Experimental Setting;** The goal of any automated method is to perform well on unseen data, with high accuracy. Therefore, we conducted a large scale study to assess how all methods generalise to new H&E stained images. To analyse the generalisation capability, we assessed the ability to segment nuclei from: i) new organs (variation in nuclei shapes) and ii) different centres (variation in staining).

Note, the four datasets used within our experiments can be grouped into two groups according to their origin: TCGA (Kumar, CPM-15, CPM-17) and TNBC. In this experiment, all methods are compared using the optimal training-testing strategy, defined in Section III-D. We used Kumar as the training and validation set, due to its size and diversity, whilst the combined CPM (CPM-15 and CPM-17) and TNBC datasets were used as two independent test sets. We split the test sets in this way in accordance with their origin. Kumar was split into three subsets as explained in Section III-A, and Kumar-Train was used to train all models, i.e. trained with samples originating from the following organs: breast; prostate; kidney and liver. Despite all samples being extracted from TCGA, CPM samples come from the brain, head & neck and lungs regions. Therefore, testing with CPM reflects the ability for the model to generalise to new organs, as mentioned above by the first generalisation criterion. TNBC contains samples from an already seen organ (breast), but the data is extracted from an independent source with different specimen preservation and staining practice. Therefore, this reflects the second generalisation criterion.

**Comparative Results;** The results are reported in Table III, where we only display the results of methods that employ an instance-based technique. We observe that our proposed model is able to successfully generalise to unseen data in both cases.

However, some methods prove to perform poorly with unseen data. In particular, DIST and Micro-Net perform poorly on data with a significantly different stain and therefore may not be successful in a practical setting.

#### F. Ablation Study

To gain a full understanding of the contribution of our method, we investigated several of its components. Specifically, we performed the following ablation experiments: (i) XY map compared to distance map (DST) as the target output of the instance branch; (ii) contribution of each loss term component and (iii) Sobel-based post-processing technique compared to other strategies. Similar to Section II, all networks were trained using Kumar-Train and analysed via the combined Kumar and TNBC datasets.

**Instance Branch;** We conducted this experiment by switching the regression target of the instance branch from XY to DST. The DST GT contains the distance map of each nuclear instance, which is normalised between 0 and 1, to match the value range of our input. A threshold applied to the predicted distance map to extract watershed markers, in place of the gradient-based processing. Both XY and DST model were trained using the most basic loss configuration, i.e  $L_a$  and  $L_c$ . We present the result in Table V. The experiment results suggest that utilising XY as a target output at the instance branch leads to a superior segmentation.

**Loss Terms;** Three experiments were conducted to analyse the contribution of each loss term. First, we used binary cross entropy loss  $L_a$  for the NP branch and mean squared error of the horizontal and vertical distances  $L_c$  for the XY branch. Within each successive experiment, we introduced Dice loss  $L_b$  to the NP branch and then mean squared error of horizontal and vertical gradients  $L_d$  to the XY branch. We present the results in Table IV. The addition of  $L_b$  improves all five measures from the baseline. In particular, it boosts the network’s ability to differentiate between nuclear and background pixels (DICE) and separate individual nuclei (SQ and PQ). We observe that, for the combined CPM and TNBC test sets, the introduction of  $L_d$  leads to a significant increase in performance and results in a sharper XY map output. We, therefore, hypothesise that  $L_d$  makes the XY prediction more resilient to unseen data. These results suggest that the proposed loss function is essential to obtain a robust instance-aware segmentation method.

**Post-Processing;** Usually, markers obtained from applying a threshold to an energy landscape (such as the distance map) is enough to provide a competitive input for watershed, as seen by DIST in Table I. However, XY is not an energy landscape. Specifically, we designed a Sobel-based method to derive both the energy landscape and the markers. To compare with other methods, we implemented two further techniques for obtaining the energy landscape and the marker. We then exhaustively compared all energy landscape and marker combinations to assess which post-processing strategy is the best. First, we start by linking XY to the distance map by calculating the square sum  $X^2 + Y^2$ , which can be seen as the inverse distance from a pixel to the nearest nuclear centroid. In other words,



TABLE IV: Ablation study with different loss terms  $L_a$ ,  $L_b$ ,  $L_c$  and  $L_d$  are defined in equations (2), (3), (4) and (5) respectively.

Loss	Kumar					CPM					TNBC				
	DICE	AJI <sup>+</sup>	DQ	SQ	PQ	DICE	AJI <sup>+</sup>	DQ	SQ	PQ	DICE	AJI <sup>+</sup>	DQ	SQ	PQ
$L_a, L_c$	0.814	0.605	0.741	0.758	0.564	0.781	0.599	0.729	0.769	0.544	0.658	0.484	0.634	0.759	0.488
$L_a, L_b, L_c$	0.824	0.616	0.759	0.765	0.583	0.789	0.617	0.747	0.788	0.591	0.675	0.503	0.645	0.764	0.505
$L_a, L_b, L_c, L_d$	0.823	0.622	0.760	0.765	<b>0.584</b>	0.810	0.643	0.774	0.782	<b>0.608</b>	0.698	0.530	0.670	0.769	<b>0.519</b>

TABLE V: Ablation study to compare XY versus Distance Map (DST). Both models were trained with  $L_a$  (binary cross entropy) and  $L_c$  (mean square error)

Loss	DICE	AJI <sup>+</sup>	DQ	SQ	PQ
NP & DST	0.807	0.574	0.726	0.761	0.555
NP & XY	0.814	0.605	0.741	0.758	<b>0.564</b>

TABLE VI: Ablation study for post-processing techniques: Sobel-based versus thresholding to get markers and Sobel-based versus naive conversion to get energy landscape

Energy	Markers	DICE	AJI <sup>+</sup>	DQ	SQ	PQ
$X^2 + Y^2$	Threshold	0.786	0.536	0.632	0.749	0.475
$X^2 + Y^2$	Sobel	0.786	0.555	0.646	0.761	0.493
Sobel	Threshold	0.823	0.614	0.755	0.757	0.574
Sobel	Sobel	0.823	0.622	0.760	0.765	<b>0.584</b>

this is a pseudo distance map. With regards to the markers, X and Y values can be interpreted as Cartesian coordinates with each nuclear centroid as the origin. By thresholding the values in between a certain range, we can obtain the markers. The results of all combinations are shown in Table VI.

#### IV. DISCUSSION

The analysis of nuclei in large-scale histopathology images is an important step towards the automated diagnosis and prognosis of cancer. For example, tumour cells are characterised by a relatively large nucleus with an irregular size and shape and with prominent nucleoli. Therefore, nuclear features have been often used to assess the degree of malignancy [41]. In addition, nuclear shape and texture varies between different types of nuclei. For instance, lymphocytes tend to have a round and heterochromatic nucleus, whereas fibroblasts have an oval shaped nucleus. However, visual analysis of the nuclei is a very time consuming procedure because there are often tens of thousands of nuclei within a given whole-slide image. We have proposed the XY-Net for accurate segmentation of nuclei within multi-tissue histology images that not only detects nuclei with high accuracy, but also effectively separates clustered nuclei. We have shown that the proposed approach achieves state-of-the-art performance across multiple datasets for several statistical measurements, including tissues that have been prepared and stained under different conditions. This makes the proposed approach potentially likely to translate well to a practical setting due its strong generalisation capacity, which can therefore be effectively used as a prerequisite

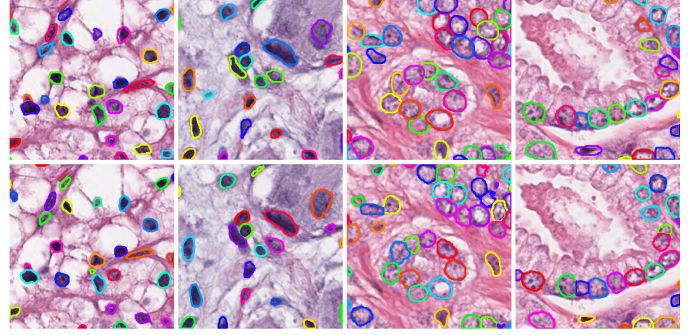


Fig. 6: Example visual results. The top row displays the ground truth, whilst the bottom row displays the output of XY-Net.

step before nuclear-based feature extraction. In the current literature, there is no known full breakdown of comparative training and testing strategies for SN and CA. We provide a comprehensive analysis that can help drive forward future research and provide insight into how to combat stain variation between images. This is, to the best of our knowledge, the most extensive work in the literature to date comparing various deep learning based nuclear segmentation methods on multiple datasets. We analysed the commonly used measures to assess the true performance of a nuclear segmentation method and discussed their limitations. In addition, we proposed a set of reliable and informative statistical measures. We encourage researchers to utilise the proposed measures to not only maximise the interpretability of their results, but also to perform a fair comparison with other methods.

#### V. CONCLUSION

In this paper, we presented an XY network for nuclear instance segmentation in multi-tissue histology images. The proposed network has two distinct up-sampling branches that each perform the two separate tasks of nuclear segmentation. The nuclear pixel branch separates nuclear pixels from the background, whereas the XY branch regresses the horizontal and vertical distances of nuclear pixels to their centres of mass. In addition, we report the effect of utilising different SN training and testing strategies. We observe that our method achieves state-of-the-art performance on two widely used multi-tissue nuclear segmentation datasets and also demonstrate the ability for our model to generalise well to new data by processing two further completely unseen datasets. Finally, we thoroughly investigate the use of current statistical measures for nuclear instance segmentation and give justification for the usage of our proposed interpretable measures for assessing the segmentation performance.

## ACKNOWLEDGMENT

This work was supported by the National Research Foundation of Korea (NRF) grant funded by the Korea government (MSIP) (No. 2016R1C1B2012433) and by the Ministry of Science and ICT (MSIT) (No. 2018K1A3A1A74065728). We thank Peter Naylor for his assistance in the implementation of the DIST network.

## REFERENCES

- [1] J. G. Elmore, G. M. Longton, P. A. Carney, B. M. Geller, T. Onega, A. N. Tosteson, H. D. Nelson, M. S. Pepe, K. H. Allison, S. J. Schnitt *et al.*, "Diagnostic concordance among pathologists interpreting breast biopsy specimens," *Jama*, vol. 313, no. 11, pp. 1122–1132, 2015.
- [2] Q. D. Vu, S. Graham, M. N. N. To, M. Shaban, T. Qaiser, N. A. Koohbanani, S. A. Khurram, T. Kurc, K. Farahani, T. Zhao *et al.*, "Methods for segmentation and classification of digital microscopy tissue images," *arXiv preprint arXiv:1810.13230*, 2018.
- [3] N. Kumar, R. Verma, S. Sharma, S. Bhargava, A. Vahadane, and A. Sethi, "A dataset and a technique for generalized nuclear segmentation for computational pathology," *IEEE Transactions on Medical Imaging*, vol. 36, no. 7, pp. 1550–1560, July 2017.
- [4] P. Naylor, M. Laé, F. Reyat, and T. Walter, "Segmentation of nuclei in histopathology images by deep regression of the distance map," *IEEE Transactions on Medical Imaging*, 2018.
- [5] A. Madabhushi and G. Lee, "Image analysis and machine learning in digital pathology: Challenges and opportunities," *Medical Image Analysis*, vol. 33, pp. 170 – 175, 2016, 20th anniversary of the Medical Image Analysis journal (MedIA). [Online]. Available: <http://www.sciencedirect.com/science/article/pii/S1361841516301141>
- [6] N. Alsabaie, K. Sirinukunwattana, S. E. A. Raza, D. Snead, and N. Rajpoot, "A bottom-up approach for tumour differentiation in whole slide images of lung adenocarcinoma," in *Medical Imaging 2018: Digital Pathology*, vol. 10581. International Society for Optics and Photonics, 2018, p. 105810E.
- [7] C. Lu, D. Romo-Bucheli, X. Wang, A. Janowczyk, S. Ganesan, H. Gilmore, D. Rimm, and A. Madabhushi, "Nuclear shape and orientation features from h&e images predict survival in early-stage estrogen receptor-positive breast cancers," *Laboratory Investigation*, vol. 98, no. 11, p. 1438, 2018.
- [8] M. Zwerger, C. Y. Ho, and J. Lammerding, "Nuclear mechanics in disease," *Annual Review of Biomedical Engineering*, vol. 13, no. 1, pp. 397–428, 2011, PMID: 21756143. [Online]. Available: <https://doi.org/10.1146/annurev-bioeng-071910-124736>
- [9] A. H. Beck, A. R. Sangoi, S. Leung, R. J. Marinelli, T. O. Nielsen, M. J. Van De Vijver, R. B. West, M. Van De Rijn, and D. Koller, "Systematic analysis of breast cancer morphology uncovers stromal features associated with survival," *Science translational medicine*, vol. 3, no. 108, pp. 108ra113–108ra113, 2011.
- [10] K. Sirinukunwattana, D. Snead, D. Epstein, Z. Aftab, I. Mujeib, Y. W. Tsang, I. Cree, and N. Rajpoot, "Novel digital signatures of tissue phenotypes for predicting distant metastasis in colorectal cancer," *Scientific reports*, vol. 8, no. 1, p. 13692, 2018.
- [11] X. Yang, H. Li, and X. Zhou, "Nuclei segmentation using marker-controlled watershed, tracking using mean-shift, and kalman filter in time-lapse microscopy," *IEEE Transactions on Circuits and Systems I: Regular Papers*, vol. 53, no. 11, pp. 2405–2414, 2006.
- [12] J. Cheng, J. C. Rajapakse *et al.*, "Segmentation of clustered nuclei with shape markers and marking function," *IEEE Transactions on Biomedical Engineering*, vol. 56, no. 3, pp. 741–748, 2009.
- [13] M. Veta, P. van Diest, R. Kornegoor, A. Huisman, M. Viergever, and J. Pluim, "Automatic nuclei segmentation in h&e stained breast cancer histopathology images," *PLoS ONE*, vol. 8, no. 7, p. e70221, 2013.
- [14] S. Ali and A. Madabhushi, "An integrated region-, boundary-, shape-based active contour for multiple object overlap resolution in histological imagery," *IEEE transactions on medical imaging*, vol. 31, no. 7, pp. 1448–1460, 2012.
- [15] S. Wienert, D. Heim, K. Saeger, A. Stenzinger, M. Beil, P. Hufnagel, M. Dietel, C. Denkert, and F. Klauschen, "Detection and segmentation of cell nuclei in virtual microscopy images: a minimum-model approach," *Scientific reports*, vol. 2, p. 503, 2012.
- [16] A. LaTorre, L. Alonso-Nanclares, S. Muelas, J. Pea, and J. DeFelipe, "Segmentation of neuronal nuclei based on clump splitting and a two-step binarization of images," *Expert Systems with Applications*, vol. 40, no. 16, pp. 6521 – 6530, 2013. [Online]. Available: <http://www.sciencedirect.com/science/article/pii/S0957417413003904>
- [17] J. T. Kwak, S. M. Hewitt, S. Xu, P. A. Pinto, and B. J. Wood, "Nucleus detection using gradient orientation information and linear least squares regression," in *Medical Imaging 2015: Digital Pathology*, vol. 9420. International Society for Optics and Photonics, 2015, p. 94200N.
- [18] M. Liao, Y. qian Zhao, X. hua Li, P. shan Dai, X. wen Xu, J. kai Zhang, and B. ji Zou, "Automatic segmentation for cell images based on bottleneck detection and ellipse fitting," *Neurocomputing*, vol. 173, pp. 615 – 622, 2016. [Online]. Available: <http://www.sciencedirect.com/science/article/pii/S09525231215011406>
- [19] G. Litjens, T. Kooi, B. E. Bejnordi, A. A. A. Setio, F. Ciompi, M. Ghafoorian, J. A. van der Laak, B. Van Ginneken, and C. I. Sánchez, "A survey on deep learning in medical image analysis," *Medical image analysis*, vol. 42, pp. 60–88, 2017.
- [20] D. Shen, G. Wu, and H.-I. Suk, "Deep learning in medical image analysis," *Annual review of biomedical engineering*, vol. 19, pp. 221–248, 2017.
- [21] Y. LeCun, Y. Bengio, and G. Hinton, "Deep learning," *nature*, vol. 521, no. 7553, p. 436, 2015.
- [22] J. Long, E. Shelhamer, and T. Darrell, "Fully convolutional networks for semantic segmentation," in *Proceedings of the IEEE conference on computer vision and pattern recognition*, 2015, pp. 3431–3440.
- [23] L.-C. Chen, G. Papandreou, I. Kokkinos, K. Murphy, and A. L. Yuille, "Deeplab: Semantic image segmentation with deep convolutional nets, atrous convolution, and fully connected crfs," *IEEE transactions on pattern analysis and machine intelligence*, vol. 40, no. 4, pp. 834–848, 2018.
- [24] H. Zhao, J. Shi, X. Qi, X. Wang, and J. Jia, "Pyramid scene parsing network," in *IEEE Conf. on Computer Vision and Pattern Recognition (CVPR)*, 2017, pp. 2881–2890.
- [25] O. Ronneberger, P. Fischer, and T. Brox, "U-net: Convolutional networks for biomedical image segmentation," in *International Conference on Medical image computing and computer-assisted intervention*. Springer, 2015, pp. 234–241.
- [26] S. E. A. Raza, L. Cheung, M. Shaban, S. Graham, D. Epstein, S. Pelen-garis, M. Khan, and N. M. Rajpoot, "Micro-Net: A unified model for segmentation of various objects in microscopy images," *ArXiv e-prints*, p. arXiv:1804.08145, Apr. 2018.
- [27] H. Chen, X. Qi, L. Yu, and P.-A. Heng, "Dcan: deep contour-aware networks for accurate gland segmentation," in *Proceedings of the IEEE conference on Computer Vision and Pattern Recognition*, 2016, pp. 2487–2496.
- [28] Y. Cui, G. Zhang, Z. Liu, Z. Xiong, and J. Hu, "A deep learning algorithm for one-step contour aware nuclei segmentation of histopathological images," *arXiv preprint arXiv:1803.02786*, 2018.
- [29] M. Khoshdeli and B. Parvin, "Deep leaning models delineates multiple nuclear phenotypes in h&e stained histology sections," *arXiv preprint arXiv:1802.04427*, 2018.
- [30] P. Naylor, M. Laé, F. Reyat, and T. Walter, "Nuclei segmentation in histopathology images using deep neural networks," in *Biomedical Imaging (ISBI 2017)*, 2017 IEEE 14th International Symposium on. IEEE, 2017, pp. 933–936.
- [31] S. Graham and N. M. Rajpoot, "Sams-net: Stain-aware multi-scale network for instance-based nuclei segmentation in histology images," in *Biomedical Imaging (ISBI 2018)*, 2018 IEEE 15th International Symposium on. IEEE, 2018, pp. 590–594.
- [32] K. He, G. Gkioxari, P. Dollár, and R. Girshick, "Mask R-CNN," *ArXiv e-prints*, p. arXiv:1703.06870, Mar. 2017.
- [33] K. He, X. Zhang, S. Ren, and J. Sun, "Identity Mappings in Deep Residual Networks," *ArXiv e-prints*, p. arXiv:1603.05027, Mar. 2016.
- [34] J. Deng, W. Dong, R. Socher, L.-J. Li, K. Li, and L. Fei-Fei, "ImageNet: A Large-Scale Hierarchical Image Database," in *CVPR09*, 2009.
- [35] A. Arnab, O. Miksik, and P. H. S. Torr, "On the robustness of semantic segmentation models to adversarial attacks," *CoRR*, vol. abs/1711.09856, 2017. [Online]. Available: <http://arxiv.org/abs/1711.09856>
- [36] G. Huang, Z. Liu, L. van der Maaten, and K. Q. Weinberger, "Densely Connected Convolutional Networks," *ArXiv e-prints*, p. arXiv:1608.06993, Aug. 2016.
- [37] "Monuseg." [Online]. Available: <https://monuseg.grand-challenge.org/>
- [38] A. Kirillov, K. He, R. B. Girshick, C. Rother, and P. Dollár, "Panoptic segmentation," *CoRR*, vol. abs/1801.00868, 2018. [Online]. Available: <http://arxiv.org/abs/1801.00868>

- [39] V. Badrinarayanan, A. Kendall, and R. Cipolla, "Segnet: A deep convolutional encoder-decoder architecture for image segmentation," *IEEE transactions on pattern analysis and machine intelligence*, vol. 39, no. 12, pp. 2481–2495, 2017.
- [40] M. Abadi, P. Barham, J. Chen, Z. Chen, A. Davis, J. Dean, M. Devin, S. Ghemawat, G. Irving, M. Isard *et al.*, "Tensorflow: A system for large-scale machine learning," in *OSDI*, vol. 16, 2016, pp. 265–283.
- [41] M. N. Gurcan, L. E. Boucheron, A. Can, A. Madabhushi, N. M. Rajpoot, and B. Yener, "Histopathological image analysis: A review," *IEEE reviews in biomedical engineering*, vol. 2, pp. 147–171, 2009.